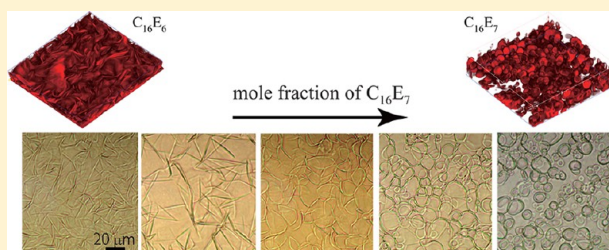


Microscopic Investigation on Morphologies of Bilayer Gel Structure in the Mixed Polyoxyethylene-Type Nonionic Surfactant Systems

Yuko Nagai,^{*,†} Youhei Kawabata,^{*,‡} and Tadashi Kato[‡][†]Kao Corporation, 2-1-3 Bunka, Sumida-ku, Tokyo 131-8501, Japan[‡]Department of Chemistry, Tokyo Metropolitan University, Hachioji, Tokyo 192-0397, Japan

Supporting Information

ABSTRACT: We investigated morphologies of lamellar domains below the Krafft temperature in the mixed polyoxyethylene-type nonionic surfactant, a $C_{16}E_6/C_{16}E_7$ /water system, by using optical microscopy, confocal microscopy, small/wide-angle X-ray scattering, and small-angle neutron scattering. We have found that the morphology discontinuously changes from network structures of lamellar domains to spherical vesicles with increasing mole fraction of $C_{16}E_7$, via the coexistence region of vesicles and network structures of lamellar domains.



INTRODUCTION

In a binary system consisting of an ionic surfactant and water, crystalline hydrated solids are deposited when the temperature decreases below the Krafft temperature, which corresponds to the melting point of the hydrophobic parts of surfactants and represents temperature-dependent equilibrium between dissolved monomers (surfactants) and the hydrated solids. In general, the hydrated solids are considered to coexist with excess water and a lamellar phase where hydrophobic tails of bilayers are a “solid-like” gel (all-trans) of L_β phase.^{1–3} For this Krafft transition, various kinds of structural formations of the L_β phase have been reported. Dubois et al. have represented regular hollow icosahedra with the gel-like bilayers in salt-free catanionic solutions below the Krafft temperature.⁴ For bilayer structures on the nanometer scale, Sasaki has found metastable crystalline lamella (L_β) in the Krafft transition of aqueous cetylpyridinium chloride solutions.⁵ With the addition of alcohol to the ionic surfactant solutions, the mixtures are sometimes strongly turbid throughout the sample without macroscopic phase separation, and they are highly viscous, a property that is applied to the cosmetic industry.⁶ In the pseudo binary systems, the lamellar domains in $\sim\mu\text{m}$ scale are dispersed in solutions with network formations.⁷ Therefore, it is important for applications in the industrial fields to investigate the structural formations of lamellar domains below the Krafft temperature.

We have discovered the new type of morphologies of the lamellar domains below the Krafft temperature in the $C_{16}E_6$ /water and $C_{16}E_7$ /water systems ($C_{16}E_m$ ($C_{16}H_{33}(OC_2H_4)_mOH$; $m = 6$ or 7), and investigated the structure formation process in the nm to μm scale using optical and confocal microscope and small-angle X-ray scattering (SAXS).^{8–10} In the $C_{16}E_6$ solution, lamellar domains are randomly arranged like “network structures”, as shown in Figure 1a. On the other hand, in the $C_{16}E_7$ system, it has been found that plate-like lamellar domains

are transformed to multilamellar vesicles with a size of $2\text{--}4\ \mu\text{m}$ (Figure 1b). These vesicles are very flexible to grow larger by fusing together, and transformation from spherical vesicles to string-like morphology occurs at a certain quench temperature.⁹ They can easily be formed, and the size and polydispersity can be controlled only by the depth of temperature quench below the Krafft temperature. Therefore, we expect the vesicles to be used for controlled drug or DNA release. As just described above, in these nonionic surfactant systems, by varying only one segment of the hydrophilic part, the morphologies of the lamellar domains are dramatically changed. Therefore, the domain morphology of their mixed systems is very interesting, and it can be a key to solve the vesicle formation mechanism. Furthermore, solving the origin of the structure formations of the lamellar domains gives us fundamental knowledge toward application of cosmetics, drug delivery, etc.

In this context, to clarify the effects of mixing $C_{16}E_6$ and $C_{16}E_7$ on the morphologies of the lamellar domains at the nm to μm scale, we have performed optical microscope, confocal microscope, SAXS, wide-angle X-ray scattering (WAXS), and small-angle neutron scattering (SANS) experiments after T-quench below the Krafft temperature in the $C_{16}E_6/C_{16}E_7$ /water systems. With increasing the hydrophilicity by adding $C_{16}E_7$, vesicles are formed at a certain mole fraction via the coexistence region of the network formations and vesicles, where the structure parameters obtained from the SAXS/WAXS and SANS also show specific behaviors. All of this experimental evidence leads us to the conclusion that the morphological transformation by the mixture of $C_{16}E_6$ and $C_{16}E_7$ cannot be explained by the change of hydrophilicity of surfactants or surfactant parameter alone, and that we should consider the

Received: June 19, 2012

Revised: September 20, 2012

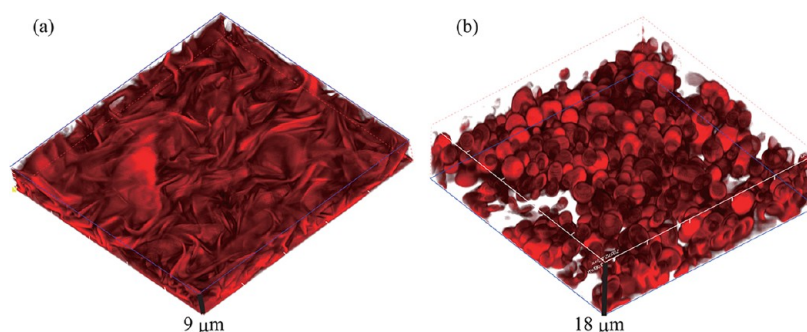


Figure 1. Confocal microscope 3D images of $C_{16}E_6$ /water (a) and $C_{16}E_7$ /water (b) systems below the Krafft temperature.

elastic energy of the lamellar phase taking into account the rim part of bilayers.

EXPERIMENTS

Samples were prepared by mixing $C_{16}E_6$ and $C_{16}E_7$ with D_2O , which were used for the neutron scattering experiments. $C_{16}E_6$ and $C_{16}E_7$ were purchased from Nikko Chemicals, Inc., in crystalline form (>98% pure) and used without further purification. Deuterated water (D_2O of 99.9 at%-D) purchased from Isotec, Inc., was used after nitrogen bubbling to avoid oxidation of the ethylene oxide group of surfactants. The total surfactant concentrations ϕ_{tot} were fixed at 10 wt % for the observation of the morphologies.

The Krafft temperatures were determined visually by changing the water bath temperature and inspecting scattered and transmitted light. The water bath temperature was controlled at a cooling rate of 0.3 K/min. The Krafft temperatures were measured by using the differential scanning calorimetry as well. The differential scanning calorimetry measurements were carried out with a DSC 6000 calorimeter (Seiko, Inc., Japan) at a heating rate of 0.5 K/min.

To observe the structure of lamellar domains below the Krafft temperature, we used an optical microscope and a confocal microscope. Optical microscope observation was performed using BX-51 (Olympus Inc.) in a wide temperature–composition range, as shown in Figure 10. Temperature was controlled by using a hotstage TMS94 LNP94/2 (Linkam Scientific Instruments Co.). The cooling rate was set to 5 K/min for all experiments. The sample thickness was less than 150 μm . The microscope images were taken with a digital video camera. Confocal microscope observation was performed using an FV-300 (Olympus Inc.). The excitation laser is a He–Ne green laser whose wavelength is 543 nm. The used fluorescence molecule was lipophilic tracers DiI (Invitrogen Inc., 1,1'-dihexadecyl-3,3,3',3'-tetramethylindocarbocyanine perchlorate, excitation and emission wavelength = 549 and 568 nm, respectively).¹⁰ Temperature was controlled by using a hotstage TS62 and controller mk-1000 (Instec Inc.) in a wide temperature range, as shown in Figure 10.

SAXS experiments were performed using the synchrotron radiation SAXS spectrometer installed in BL-15A at the Photon Factory (PF) of the High Energy Accelerator Research Organization (KEK), Tsukuba. The scattering X-rays were detected with a CCD camera, C7300 with 9 in. Image Intensifier (Hamamatsu Photonics Inc.). The scattering vector $q = 4\pi \sin \theta / \lambda$ (where 2θ is the scattering angle and λ is the X-ray wavelength, 0.15 nm) range is from 0.5 to 2.5 nm^{-1} . The energy resolution $\Delta E/E$ is 3×10^{-3} . The scattering intensity was measured with an exposure time of 5 s. The sample cell is

made of copper with Kapton windows, and the temperature of the sample was controlled using the DTA/SAXS instrument with a precision of 0.1 $^{\circ}C$.¹¹

WAXS experiments were performed by using NANO-Viewer (Rigaku Inc.). The scattered X-ray was detected by an imaging plate. The q range is 10–35 nm^{-1} . The sample cell is made of copper with Kapton windows, and the temperature of the sample was controlled by using TS-62 and mk-1000 controller with a precision of ± 0.1 $^{\circ}C$. The temperature quench depth was 8 $^{\circ}C$ for all samples.

The SANS experiments were conducted with the SANS-U spectrometer in JRR-3M, Tokai, Japan. The wavelength of the incident neutron beam was 0.7 nm, with a spread of $\delta\lambda/\lambda \sim 10\%$ (full width at half-maximum). The distance from the sample to a two-dimensional position-sensitive detector was 12 m, and the covered q range was 0.015 to 0.210 nm^{-1} . The sample cell is made of quartz, and the sample thickness is 1 mm. The sample temperature was controlled by a water bath circulator. The temperature quench depth was 8 $^{\circ}C$ for all samples.

RESULTS AND DISCUSSION

Krafft Temperature. Figure 2a represents visual observation images of the sample of $\gamma_{E7} = 0.8$ around the Krafft temperature, where γ_{E7} is the mole fraction of $C_{16}E_7$ in the mixed surfactant. In this case, the Krafft temperature was determined to be 14.85 $^{\circ}C$ where the solution becomes turbid. Figure 2b shows the endothermal DSC curves for different γ_{E7} . With increasing mole fraction of $C_{16}E_7$, endothermal peak shifts to the lower temperature. Figure 2c represents the Krafft temperature as a function of the mole fraction of $C_{16}E_7$ at a total surfactant concentration of 10 wt %. The open squares and the filled circles show the Krafft temperatures determined by visual observations and DSC, respectively. For the DSC curve, the Krafft temperature was determined by the crossing point of the linear dropping part of the peak and the background average. These two sets of data are in good agreement. It can be seen from the figure that the Krafft temperature decreases monotonously with increasing γ_{E7} .

SAXS/WAXS and SANS Experiments. Figure 3a and b show typical SAXS profiles of $C_{16}E_6$ / $C_{16}E_7$ /water systems at 1200 s after T-quench and the repeat distance d of the lamellar structure (L_p), respectively. The repeat distance was obtained from the position q_0 of the second-order diffraction peak at around $q = 1.6$ nm^{-1} in the composition range $\gamma_{E7} = 0.8$ –1.0, because the first-order peak intensity is very weak. This tendency of the SAXS profiles that the second-order peak is more pronounced than the first peak can be found in the pure $C_{16}E_7$ /water system as well. In our previous study,⁸ we have

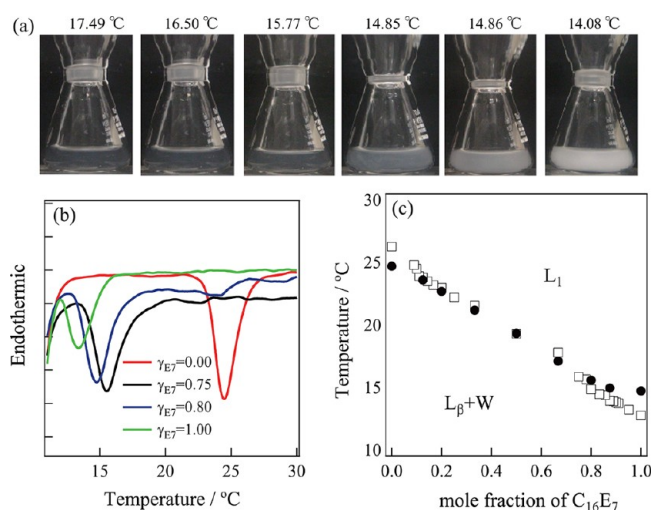


Figure 2. (a) Images for visual observation of the sample of C₁₆E₇ mole fraction $\gamma_{E7} = 0.8$ around the Krafft temperature. The Krafft temperature was determined to be 14.85 °C where the solution becomes turbid. (b) Typical DSC curves of C₁₆E₆/C₁₆E₇/water systems. The endothermic peak position at $\gamma_{E7} = 0$, which corresponds to the Krafft temperature, shifts to the lower temperature with increasing mole fraction of C₁₆E₇. (c) Phase diagram of the pseudo-binary system C₁₆E₆/C₁₆E₇/water at a total surfactant concentration of 10 wt %. The open squares show the Krafft temperature determined visually, and the filled circles indicate the temperature measured by DSC.

succeeded to analyze the SAXS profile by using the scattering function for the lamellar structure,¹² which can be generally used for various lamellar systems. This indicates that the enhancement of the second peak is due to the form factor of bilayers.

As shown in Figure 3b, the repeat distance increases with increasing mole fraction of C₁₆E₇ up to $\gamma_{E7} = 0.75$, where it takes a maximum. Then, the repeat distance decreases again with increasing γ_{E7} . It should be noted that the peak intensity decreases with increasing γ_{E7} and that the peak at around $\gamma_{E7} =$

0.75 is very weak and broad. If this peak broadening is due to the fluctuation of lamellar structures, the increase in the repeat distance with increasing γ_{E7} is consistent with the decrease in the peak intensity. Sanfinya et al. have proved on the basis of the theoretical and experimental analysis that the fluctuation of layers and the peak broadening are enhanced with increasing repeat distance when the Helfrich interaction plays a major role in the interlayers.¹³ For our case, repeat distance increases up to ~9 nm with increasing C₁₆E₇ fraction up to 0.8. To keep the large repeat distance, therefore, the fluctuation should be enhanced.

In order to discuss the behavior of the repeat distance, we have determined the phase boundary between the L_β and L_β + W phases at several mole fractions of C₁₆E₇ on the basis of the dependence of d on the total surfactant concentration and the swelling law of the lamellar phase¹⁴

$$d = \delta_{hc} \phi_{hc}^{-1} \quad (1)$$

where δ_{hc} and ϕ_{hc} are the thickness and volume fraction of the hydrophobic part of bilayers, respectively. Equation 1 indicates that a plot of $\log d$ vs $\log \phi_{hc}$ gives a straight line with a slope of -1 . Parts a and b of Figure 4 show such a double logarithmic plot obtained at 15.2 °C and $\gamma_{E7} = 0.5$ and at 10.5 °C and $\gamma_{E7} = 0.83$, respectively. The volume fraction ϕ_{hc} is calculated from the weight fraction and the volume of each functional group of the surfactant using the empirical equations reported previously.¹⁵

The slope of the dashed line in each panel was fixed to be -1 , and by using eq 1, δ_{hc} at $\gamma_{E7} = 0.5$ and 0.83 were obtained to be 2.50 ± 0.01 and 2.07 ± 0.19 nm, respectively, which are consistent with the extended length of alkyl chains estimated from Tanford's relation, 2.17 nm,¹⁶ taking into account the interdigitated structure of the L_β phase. We determined the phase boundary from ϕ_{hc} where the repeat distance deviates from the straight line. The phase boundaries of other temperatures for $\gamma_{E7} = 0.5$ and 0.83 were estimated by using eq 1 and the temperature dependence of the repeat distance at $\phi_{tot} = 50$ and 40 wt %, respectively, assuming that δ_{hc} does not depend on the temperature. The detailed procedure of

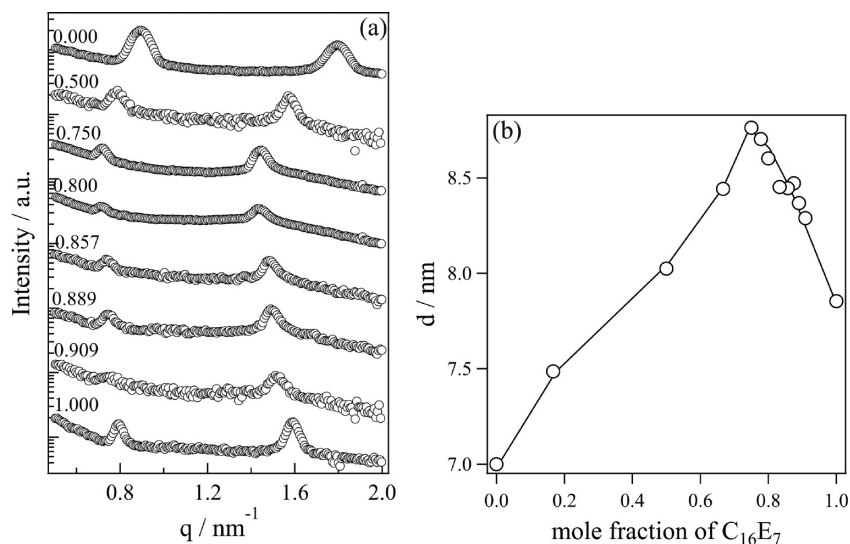


Figure 3. (a) Typical SAXS profiles of C₁₆E₆/C₁₆E₇/water systems and (b) dependence of the repeat distance d on the mole fraction of C₁₆E₇, γ_{E7} . The repeat distance does not increase monotonously with increasing mole fraction of C₁₆E₇ and takes a maximum at $\gamma_{E7} = 0.750$ where the intensity of the Bragg peak becomes very weak.

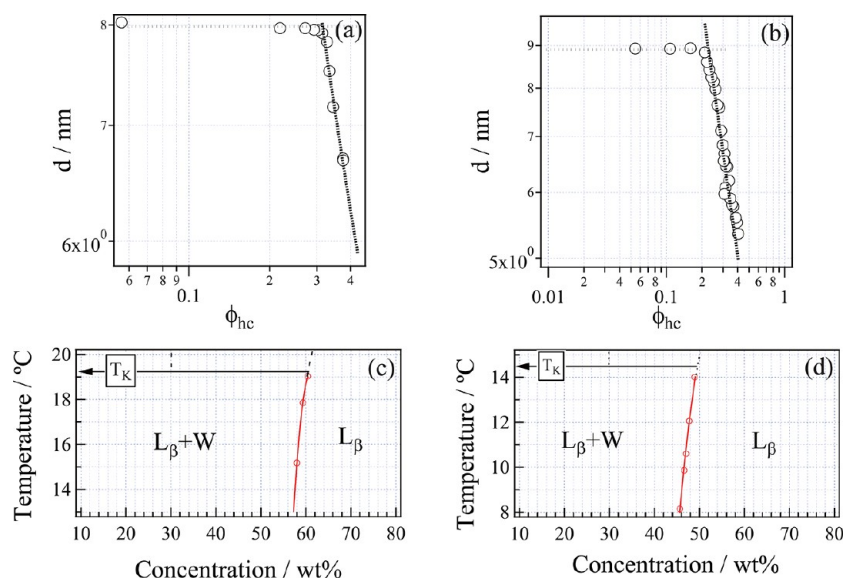


Figure 4. d – ϕ_{hc} double logarithmic plots (a and b) obtained at 15.2 °C and $\gamma_{E7} = 0.5$ and at 10.5 °C and $\gamma_{E7} = 0.83$, respectively. Straight lines are the fitting results, whose slopes are -1 . ϕ_{hc} is the volume fraction of hydrophobic chains. The partial phase diagrams (c and d) were made on the basis of the d – ϕ_{hc} plot, for $\gamma_{E7} = 0.5$ and 0.83, respectively.

determination of the phase boundary is shown in the Supporting Information. The obtained partial phase diagrams are shown in Figure 4c and d, corresponding to $\gamma_{E7} = 0.5$ and 0.83, respectively. It is obvious that the lower limit of the L_β phase at $\gamma_{E7} = 0.83$ is smaller than that at $\gamma_{E7} = 0.5$. Therefore, the increase of the repeat distance with increasing γ_{E7} corresponds to the swelling of the L_β phase. This may be a result from the fact that more water molecules can be included between bilayers as the fraction of the more hydrophilic component ($C_{16}E_7$) increases. Furthermore, taking into account the peak broadening of the SAXS profiles, this phase behavior may be due to the enhancement of the fluctuation of bilayers. In order to confirm this scenario, we performed the WAXS experiments.

Figure 5 shows the obtained WAXS profiles. The Bragg peaks at around $q = 15 \text{ nm}^{-1}$ correspond to hexagonally ordered structures in the bilayer plane, and the distance between alkane tails is 0.42 nm. The peak positions do not change with increasing γ_{E7} , but the peak becomes broader as γ_{E7} increases. Figure 6 shows the peak width estimated from the fitting by using the Gaussian function. The peak broadening indicates that the molecular packing becomes loose (more disordered). As a result, the bending rigidity may decrease, which enhances the fluctuation of bilayers. We have considered that the increase of the repeat distance may be due to the enhancement of the fluctuation of bilayers. On the other hand, for the higher γ_{E7} (>0.8), the width of the WAXS peak decreases a little bit with increasing $\gamma_{E7} = 1$. Therefore, the decrease of the repeat distance may be due to the suppression of the fluctuation of bilayers. However, the decrease of the peak width is unusual because the hydrophilic group become more bulky with increasing γ_{E7} .

Figure 7 shows the typical SANS profiles in the low q region at 1800 s after T-quench. The scattering intensity in this q region (0.02 – 0.2 nm^{-1}) reflects the internal structures of lamellar domains because the thickness of the lamellar domain size (layer stack size) is sub-micrometer up to $1 \mu\text{m}$. It can be seen from Figure 7 that the SANS profiles follow the power law, $\sim q^{-\alpha}$. The power law index α is approximately 4–5.

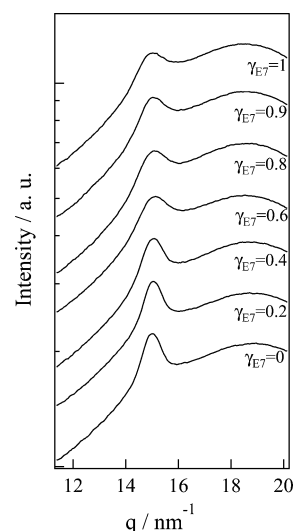


Figure 5. The obtained WAXS profiles at each γ_{E7} . The temperature quench depth was 8 °C for all samples. The Bragg peaks at around $q = 15 \text{ nm}^{-1}$ correspond to hexagonal order of surfactants in the bilayer plane, and $d = 0.42 \text{ nm}$. The peak positions do not change with increasing γ_{E7} , but the peak becomes broader with increasing γ_{E7} .

Taking into account this q dependence, the SANS profiles have been analyzed by using two models. One is the modified Porod law proposed by Strey et al.¹⁷ Since the thickness of the domain is sub-micrometer to $\sim \mu\text{m}$, there is no wonder even if the Porod law holds in the above q region. Another one is the Teubner–Strey model usually applied to microemulsion systems.¹⁸

The blue lines of Figure 7 are the fitting results with the modified Porod law¹⁷

$$I(q) = A \exp(-q^2 t^2) / q^4 \quad (2)$$

where t is the thickness parameter for the diffused interface. The red lines are the fitting results based on the Teubner–Strey model

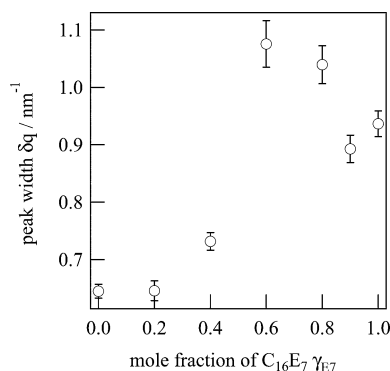


Figure 6. The peak width obtained from fitting of the WAXS peak using the Gaussian function (the instrumental resolution is not taken into account).

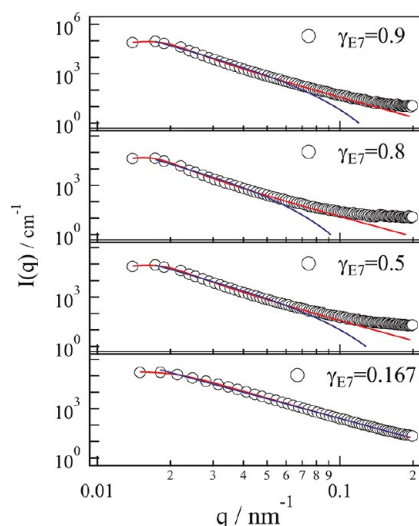


Figure 7. Typical SANS profiles of $C_{16}E_6/C_{16}E_7$ /water systems. The blue and red lines are fitting results based on eqs 2 and 3, respectively.

$$I(q) = \frac{1}{a_2 + c_1 q^2 + c_2 q^4} \quad (3)$$

where a_2 , c_1 , and c_2 are parameters related to the correlation length ξ and the quasi-periodic repeat distance d_{TS} by the following equations

$$\xi = \left[\frac{1}{2} \left(\frac{a_2}{c_2} \right) + \frac{c_1}{4c_2} \right]^{-1/2} \quad (4)$$

$$d = 2\pi \left[\frac{1}{2} \left(\frac{a_2}{c_2} \right) - \frac{c_1}{4c_2} \right]^{-1/2} \quad (5)$$

For the lower γ_{E7} , the SANS profiles are well explained by the modified Porod law, but for the higher γ_{E7} , the fitting curves are deviated from the observed SANS profiles at higher q . On the other hand, the Teubner–Strey model can explain the observed profiles better than the modified Porod law. Figure 8 shows γ_{E7} dependences of the obtained parameters for these two models. It can be seen from Figure 8a that the parameter A decreases with increasing γ_{E7} up to 0.8, whereas t increases. Because the scattering length density depends on γ_{E7} only slightly, A is proportional to the area of the interface per volume.¹⁷ Thus, the decrease of A corresponds to the domain coarsening. The

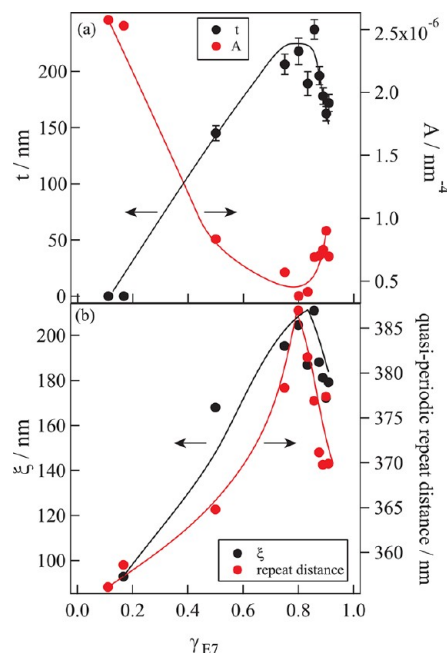


Figure 8. γ_{E7} dependences of the parameters obtained from the analyses of SANS profiles (Figure 7). (a) The parameters A and t obtained by using the modified Porod law.¹⁷ t is the thickness parameter for the diffused interface, and A is proportional to the area of the interface per volume. (b) The correlation length ξ and the quasi-periodic repeat distance d_{TS} calculated from the fitting parameters obtained by using the Teubner–Strey model.¹⁸

increase of t indicates that the interface of the domain becomes more diffuse. However, this model cannot explain the observed scattering curves especially at high- q region, as is seen from Figure 7. Thus, we do not discuss these results further.

Figure 8b shows that both the correlation length ξ and the quasi-periodic repeat distance d_{TS} increase with increasing γ_{E7} and take maxima at $\gamma_{E7} \sim 0.8$, which are again consistent with the domain coarsening. It should be noted however that d_{TS} is much smaller than the distance between the lamellar domains observed by optical microscope which is larger than a few μm (see Figures 1, 9, 10, 11, and 13). Thus, these results may suggest that there exist subdomains in the lamellar domains and that these subdomains grow with increasing γ_{E7} up to 0.8. Such a growth of subdomains may be correlated with the transition from the networks to the vesicles, although we have no definite picture about the subdomains at present.

Figure 8a and b demonstrates that all the parameters obtained from these two models take a maximum or minimum at $\gamma_{E7} \sim 0.8$, which suggests that the domain structure of sub- μm scale may also change at about 0.8.

Thus, all the scattering results suggest that the structures in the nm to sub- μm scale do not change monotonously with increasing γ_{E7} and that they abruptly change at $\gamma_{E7} \sim 0.8$.

Optical Microscope Experiments. Figure 9 shows optical microscope images of the $C_{16}E_6/C_{16}E_7$ /water systems at 1200 s after T-quench. All images were obtained 6 °C below the Krafft temperature. It can be obviously found that the morphology changes with increasing mole fraction of $C_{16}E_7$. We investigated the composition dependence of the lamellar domain morphology at other temperatures and made a morphological diagram, as shown in Figure 10.

The lamellar domain morphologies were mainly classified into five groups, as described in the top figure. In the region of

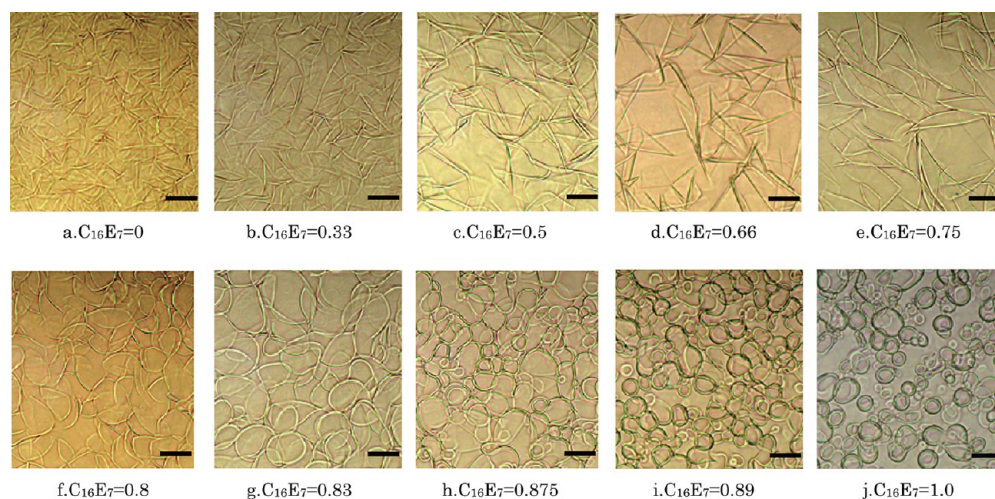


Figure 9. Optical microscope images of the $C_{16}E_6/C_{16}E_7$ /water system (the total surfactant concentration is 10 wt %) at 1200 s after T-quench. The morphology changes from network structures, membrane-like structures, membrane-like structures coexisting with vesicles, and to vesicles, depending on the mole fraction of $C_{16}E_7$. The scale bars are 20 μm .

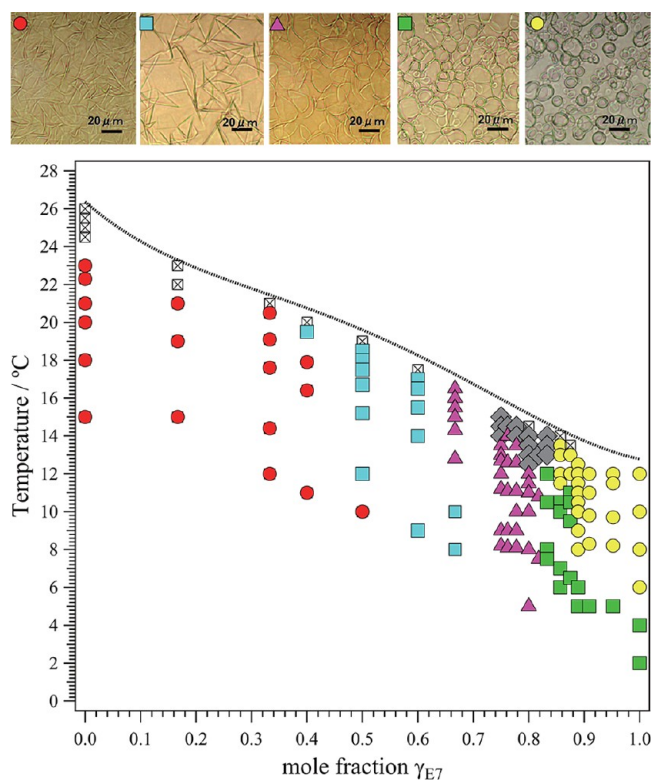


Figure 10. The morphological diagram of lamellar domains below the Krafft temperature. The lamellar domain morphologies are mainly classified into five groups as described in the top figure. In the region of $\gamma_{E7} = 0-0.33$ (Figure 9a,b), the lamellar domains are randomly arranged (red circles in Figure 10). From the mole fraction from 0.5 to 0.75 (Figure 9c–e), the lamellar domain network is coarsened (blue squares), and from 0.65 to 0.8 (Figure 9f), they are entangled with each other with curved curvature (purple triangles). Between 0.8 and 0.875, many lamellar domains with spherical forms are close-packed (yellow circles). Over the mole fraction $\gamma_{E7} = 0.9$, vesicles were clearly seen (Figure 9i,j). Around $\gamma_{E7} = 0.8$, as shown in Figure 11, there is a coexistence region of vesicles and randomly arranged layers, as shown in the gray squares of Figure 10.

$\gamma_{E7} = 0-0.33$ (Figure 9a and b), the lamellar domains are randomly arranged (red circles in Figure 10). From the mole

fraction from 0.5 to 0.75 (Figure 9c–e), the lamellar domain network is coarsened (blue squares), and from 0.65 to 0.8 (Figure 9f), they are entangled with each other with a certain curvature (purple triangles). Between $\gamma_{E7} = 0.8$ and 0.875, many lamellar domains with spherical forms are close-packed (yellow circles). Over the mole fraction $\gamma_{E7} = 0.9$, vesicles were clearly seen (Figure 9i and j). Around $\gamma_{E7} = 0.8$, as shown in Figure 11,

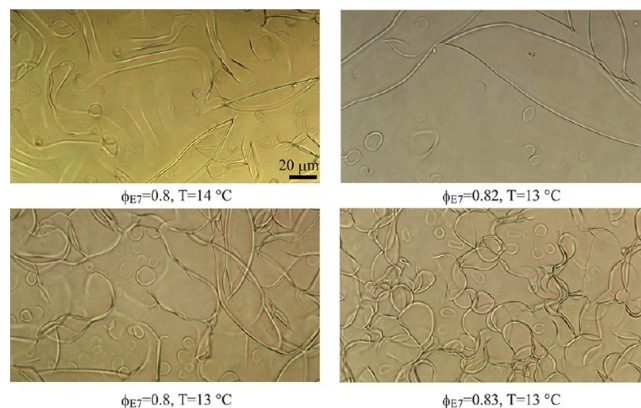


Figure 11. Typical images of the coexistence state of vesicles and randomly arranged layers observed in the region marked by gray squares in Figure 10.

there is a coexistence region of vesicles and randomly arranged layers, as shown in the gray squares of Figure 10. This region corresponds to the boundary between the vesicle region and the network-like structure region.

In order to inspect this morphological change quantitatively, we analyzed the circularity of the lamellar domain morphologies by using Image J.¹⁹ Circularity is defined as $4\pi a/L^2$. Here, a and L are the area and boundary length of spheres, respectively. In the case of complete spheres, the value of the quantity circularity is unity. As shown in Figure 12, the circularity is about 0.15 below the mole fraction of $C_{16}E_7$ around 0.75. However, it increases abruptly at $\gamma_{E7} \sim 0.8$. As γ_{E7} increases above 0.85, the circularity changes gradually to unity. These results suggest that the morphological change between network structures and vesicles occurs abruptly and there might be some

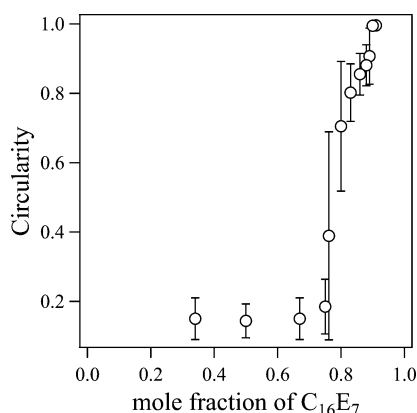


Figure 12. Effects of the mole fraction of C₁₆E₇ γ_{E7} on the circularity of the morphology. Circularity increases up to 1 with increasing mole fraction of the C₁₆E₇.

intermediate region where network structures and vesicles coexist at around $\gamma_{E7} = 0.8$.

Confocal Microscope Experiments. In order to inspect the lamellar domain structures in more detail, we observed the three-dimensional morphologies by confocal microscope. Figure 13 shows typical 3D images and their XY slice images of the mixed surfactant systems, whose mole fractions of C₁₆E₇ γ_{E7} are 0.60, 0.75, 0.80, and 0.875. At $\gamma_{E7} = 0.60$, lamellar domain structures are randomly arranged and form network structures. At $\gamma_{E7} = 0.75$, each lamellar domain becomes round and is randomly arranged. At $\gamma_{E7} = 0.8$, vesicles coexist with the network-like structures. As the mole fraction approaches unity, the lamellar domain becomes spherical vesicles. It should be emphasized that the morphology of the lamellar domains in the C₁₆E₆/C₁₆E₇/water changes dramatically at $\gamma_{E7} \sim 0.8$, where vesicles coexist with the network structures. This result is consistent with the microscope observations, where the circularity changes discontinuously at $\gamma_{E7} \sim 0.8$.

DISCUSSION

From the microscope observations, we have found that the lamellar domain does not continuously change from the

network structure to the spherical vesicles with increasing C₁₆E₇ fraction but abruptly changes via coexistence region at the C₁₆E₇ mole fraction around 0.8. Also, the SAXS and SANS results suggest that the lamellar structures both in the nm and sub- μ m scales change at $\gamma_{E7} \sim 0.8$, and that the structural parameter, such as repeat distance, does not monotonously vary with increasing γ_{E7} . From all of these experimental results, we have concluded that the morphological transformation and the local structures of the L _{β} phase in the mixtures of C₁₆E₆ and C₁₆E₇ cannot be interpreted by the change of hydrophilicity of surfactants alone.

Because the lamellar domains exist in nonequilibrium states, we should consider the kinetic aspects of formation of bilayers. In our previous paper,⁸ we have shown the time evolution of confocal microscope images in pure C₁₆E₆ or C₁₆E₇ aqueous solutions. From these results, we have found the following results.

- In the C₁₆E₆ system, small discotic lamellar domains which appear just after the T-quench rapidly grow up keeping their shape, and then they fuse together without closing themselves.
- In the C₁₆E₇ system, the small domains gradually grow up to the plate-like discoid layers, and they are closed to become spherical vesicles slowly for about 10 min.

The domain growth rate is considered to depend on the instability of the rim part of lamellar domains. One of the possible geometries of the rim part is the curved multilamellar cylindrical bridge, as shown in Figure 14. Then, the energy of rim part, i.e., line tension, is proportional to the bending modulus of bilayers.

Since the WAXS results suggest that bilayers become more flexible with increasing γ_{E7} , the line tension decreases. For the lower γ_{E7} , domains rapidly grow. Furthermore, the discoid domains cannot bend themselves due to their large bending modulus, and they fuse each other to reduce the rim energy and form the network structures, as shown in Figure 15a. When γ_{E7} exceeds 0.8, the discoid domains do not grow larger and they are kept for longer time than that in the C₁₆E₆ system because the rim energy is relatively low. To reduce the rim energy, the

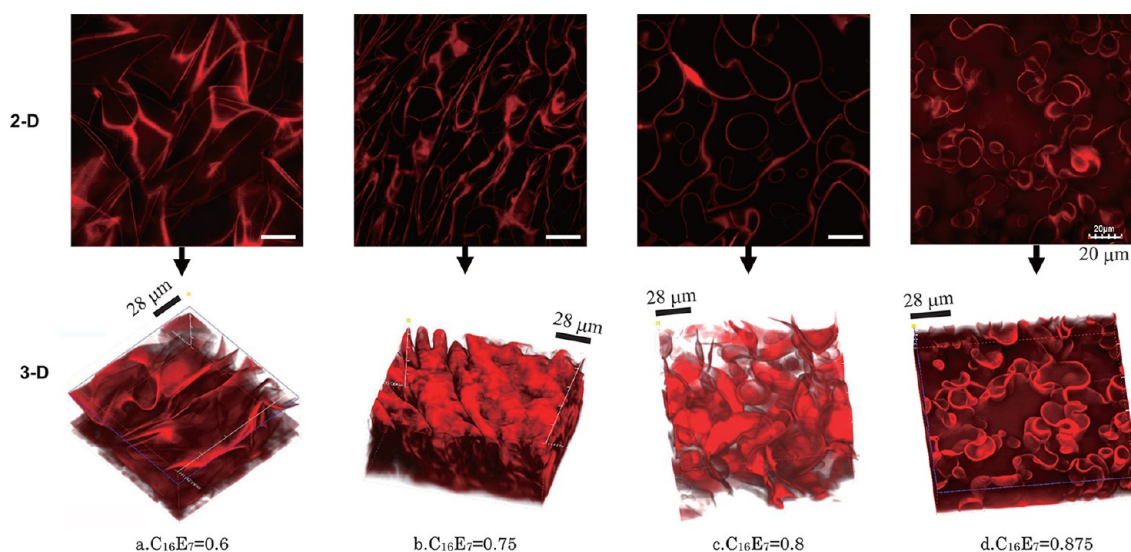


Figure 13. Confocal microscope 2-D and 3-D images of the C₁₆E₆/C₁₆E₇/water system at 1200 s after T-quench to 6 °C below the Krafft temperatures of each sample.

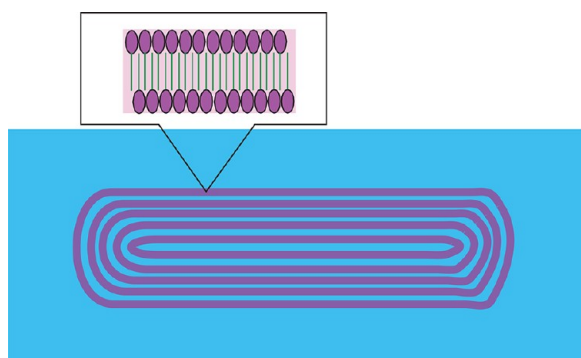


Figure 14. The schematic images of the discoid lamellar domain. The rim part is considered as the curved multilamellar morphologies.

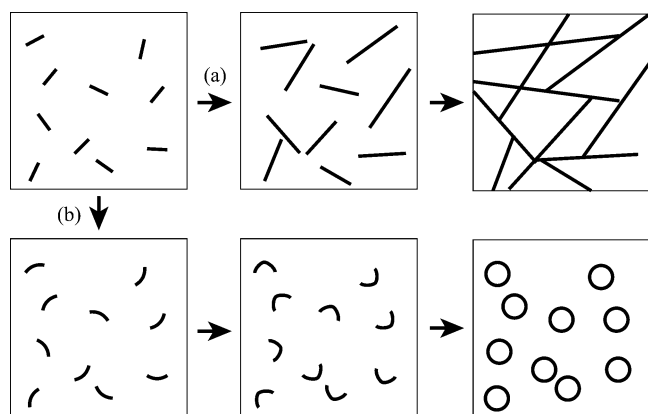


Figure 15. Schematic model for formation of the lamellar domain morphologies for the $C_{16}E_6$ or $C_{16}E_7$ /water system. Pathway a corresponds to the formation kinetics of the network structures observed below $\gamma_{E7} \sim 0.8$. In the case of highly hydrophobic bilayers, the domain coarsening may be enhanced due to high line tension. On the other hand, above $\gamma_{E7} \sim 0.8$, the line tension may be lower than that in the $C_{16}E_6$ system. Because the domains cannot fuse with each other, the flexible layers are closed to form vesicles to reduce the rim energy.

flexible layers in the $C_{16}E_7$ system are closed to form vesicles, as shown in Figure 15b. However, we cannot explain the vesicle formation by the above scenario, and competition between the line tension and the bending elasticity of the lamellar domains should be considered.

For vesicle formations, some theoretical models have been reported. In these models, the free energy of unilamellar vesicle formation is considered as a sum of two energy terms, i.e., rim and bending energies of a plate-like bilayer.^{20,21} When the rim energy is higher or the bending energy is lower, a vesicle can be formed to reduce the rim part. Because vesicles in our system are multilamellar ones and the high bending modulus of the bilayers in the gel state is predicted, this model might not always be applied to our system. Therefore, we estimated the bending modulus by using the procedure proposed by Safinya et al.¹³ The detailed procedure has been described in the Supporting Information. From this analysis, we obtained the bending modulus of a few $k_B T$, which is much smaller than expected for the gel state. Therefore, surprisingly, the bilayers are flexible in spite of their gel structures. We have considered that this feature may be due to large and flexible hydrophilic segments of surfactant molecules, which leads to the flexible morphology such as vesicles. If the bending modulus is very

high, bilayers cannot bend themselves to form vesicles. Therefore, the bending modulus in the order of $k_B T$ may be reasonable, although its absolute value is arguable.

If this vesicle formation model is correct for our results, coexistence of vesicle and plate may occur at a certain mole fraction. The coexistence of vesicle and network at $\gamma_{E7} \sim 0.8$ may correspond to that of vesicle and “plate” in the model. The network structure is not exactly “plate”, but they are common structures in the layers with small curvature. Therefore, we have considered this scenario might be qualitatively correct.

CONCLUSION

In this study, we have found the morphological variations of the lamellar domains below the Krafft temperature in the $C_{16}E_6$ / $C_{16}E_7$ /water systems, by using optical microscope, confocal microscope, SAXS/WAXS, and SANS. From the SAXS experiments, it has been found that repeat distance takes a maximum at the mole fraction $\gamma_{E7} \sim 0.75$. The SANS profiles follow the power law, and we have analyzed them using two different models. All the scattering results suggest that the structures in the nm to sub- μm scale do not change monotonously with increasing γ_{E7} and that they abruptly change at $\gamma_{E7} \sim 0.8$. From the microscope observation, we have made the morphological diagram in the wide range of temperature and mole fraction of $C_{16}E_7$. The morphology of lamellar domains abruptly changes and the circularity begins to increase at $\gamma_{E7} \sim 0.8$, where the vesicle and lamellar domain network structures coexist. All of this experimental evidence leads us to the conclusion that the morphological transformation in the mixture of $C_{16}E_6$ and $C_{16}E_7$ cannot be explained by the change of the hydrophilicity of surfactants or surfactant parameter alone, and that we should consider the elastic energy of the lamellar phase taking into account the rim part of the lamellar domains. This fundamental knowledge might be a great help for the application of vesicles formed via Krafft transition to the material capture/release system, drug delivery, and so on.

ASSOCIATED CONTENT

Supporting Information

The procedure to make the phase diagram and the examination for the bending modulus of bilayers. This material is available free of charge via the Internet at <http://pubs.acs.org>.

AUTHOR INFORMATION

Corresponding Author

*E-mail: nagai.yuko@kao.co.jp (Y.N.); youheik@tmu.ac.jp (Y.K.). Phone: +81-3-5630-9479 (Y.N.); +81-42-677-1111 (Y.K.). Fax: +81-3-5630-9342 (Y.N.); +81-42-677-2525 (Y.K.).

Notes

The authors declare no competing financial interest.

ACKNOWLEDGMENTS

This work was supported by KAKENHI 18068016 (Grant-in-Aid for Scientific Research on Priority Area “Soft Matter Physics”) and 21740314 (Grant-in Aid for Young Scientists (B)) from the Ministry of Education, Culture, Sports, Science and Technology of Japan. SAXS and SANS experiments have been performed under the approval of Photon Factory Program Advisory Committee (Proposal No. 2008G135) and under the Joint-use Research Program for Neutron Scattering, Institute

for Solid State Physics (ISSP), the University of Tokyo, at the Research Reactor JRR-3, JAEA (Proposal No. 8611).

■ REFERENCES

- (1) Kunieda, H.; Shinoda, K. *J. Phys. Chem.* **1976**, *80*, 2468–2470.
- (2) Shinoda, K.; Yamaguchi, N.; Carlsson, A. *J. Phys. Chem.* **1989**, *93*, 7216–7218.
- (3) Laughlin, R. G. *The Aqueous Phase Behavior of Surfactants*; Academic Press: London, U.K., 1994.
- (4) Dubois, M.; Demé, B.; Krzywicki, T. G.; Dedieu, J. C.; Vautrin, C.; Désert, S.; Perez, E.; Zemb, T. *Nature* **2001**, *411*, 672–675.
- (5) Sasaki, S. *J. Phys. Chem. B* **2007**, *111*, 8453–8458.
- (6) Akatsuka, H.; Ohara, Y.; Otsubo, Y. *J. Colloid Interface Sci.* **2006**, *302*, 341–346.
- (7) Yamagata, Y.; Senna, M. *Langmuir* **1999**, *15*, 4388–4391.
- (8) Kawabata, Y.; Matsuno, A.; Shinoda, T.; Kato, T. *J. Phys. Chem. B* **2009**, *113*, 5686–5689.
- (9) Kawabata, Y.; Shinoda, T.; Kato, T. *Phys. Chem. Chem. Phys.* **2011**, *13*, 3484–3490.
- (10) Kawabata, Y.; Yashima, H.; Kato, T. *J. Phys. Chem. B* **2012**, *116*, 1593–1597.
- (11) Yoshida, H.; Kinoshita, R.; Teramoto, Y. *Thermochim. Acta* **1995**, *264*, 173–183.
- (12) Nallet, F.; Laversanne, R.; Roux, D. *J. Phys. II* **1993**, *3*, 487–502.
- (13) Safinya, C. R.; Roux, D.; Smith, S.; Sinha, S. K.; Dimon, P.; Clark, N. A. *Phys. Rev. Lett.* **1986**, *57*, 2718–2721.
- (14) Luzatti, V. In *Biological Membranes*; Chapman, D., Ed.; Academic Press: London, 1968; pp 71–123.
- (15) Minewaki, K.; Kato, T.; Yoshida, H.; Imai, M.; Ito, K. *Langmuir* **2001**, *17*, 1864–1871.
- (16) Tanford, C. *The Hydrophobic Effect: Formation of Micelles and Biological Membranes*; Wiley: New York, 1980.
- (17) Strey, R.; Winker, J.; Magid, L. *J. Phys. Chem.* **1991**, *95*, 7502–7507.
- (18) Teubner, M.; Strey, R. *J. Chem. Phys.* **1987**, *87*, 3195–3200.
- (19) Abramoff, M. D.; Magelhaes, P. J.; Ram, S. J. *Biophotonics Int.* **2004**, *11*, 36–42.
- (20) Fromherz, P. *Chem. Phys. Lett.* **1983**, *94*, 259–266.
- (21) Shioi, A.; Hatton, T. A. *Langmuir* **2002**, *18*, 7341–7348.